

***Ab initio* Surface Phase Diagram of Sn/Cu(001): Reconciling Experiments with Theory**

Ji-Hwan Lee, Jongmin Yun, Taehun Lee, and Aloysius Soon*

Department of Materials Science and Engineering, Yonsei University, Seoul 03722, Korea
(Received 15 June 2017; revised manuscript received 1 August 2017; published 15 September 2017)

Despite numerous experimental and theoretical studies on the highly miscible Sn/Cu(001) system, a conclusive detailed atomic picture of this rich alloy surface phase diagram is still warranted. Depending on the surface coverage of Sn, a rich variety of Sn/Cu(001) surface structures may be expected, ranging from the so-called phase I to phase IV. An extreme lack of atomic details about them hinders the overall comprehension of this alloy system. We focus on examining the surface energetics and thermodynamics of the Sn/Cu(001) structures to identify the low-energy structures for the experimentally observed phases I–IV. We also discuss the surface electronic structure of these low-energy Sn/Cu(001) structures in terms of their surface work functions and surface dipole moments. Finally, we compare the simulated scanning-tunneling-microscopy (STM) images of these Sn/Cu(001) phases with available experimental STM measurements. We believe this work sets a good theoretical platform for an accurate further investigation of the Sn/Cu bimetallic surface-alloy system for surface-sensitive applications in, e.g., heterogeneous nanocatalysis.

DOI: [10.1103/PhysRevApplied.8.034010](https://doi.org/10.1103/PhysRevApplied.8.034010)**I. INTRODUCTION**

Despite numerous experimental and theoretical studies on metal alloys and their surfaces, much is left to explore with regards to their structure-property relations for modern technology applications in, e.g., the areas of lithium-ion batteries [1,2], surface functionalization for molecular detection [3], electronic devices [4], and technical heterogeneous catalysis [5–8]. Metal alloys (especially at their surfaces) can exhibit a wide range of interesting and unique atomic structures depending greatly on their miscibility. For low-miscibility systems, both homogeneous and heterogeneous adatom-substrate surface structures have been reported [9], while those with high miscibility and more complex and complicated surface structures may arise, forming anywhere between sandwichlike multilayers and heavily reconstructed pseudomorphic surface-alloy structures [9,10].

In this regard, Sn/Cu(001)—a bimetallic alloy system with a high miscibility—shows a rather rich (and complex) surface phase space in terms of both atomic and electronic structures, where their surface chemistry can be exploited for specific applications. For instance, the addition of Sn to the Cu surface was found to be crucial in the self-formation of two-dimensional supramolecular nanostructures [3]. Here, the introduction of Sn to Cu(001) plays a key role in the inhibition of the (unwanted) deprotonation reaction on this surface. This Sn/Cu system was also recently proposed as a promising selective catalyst for the electroreduction of CO₂ where the pristine metals (i.e., Cu and Sn)

fail to reduce CO₂ selectively [11,12]. The surface-modified Sn/Cu nanocatalyst shows superior selectivity and activity, as well as high durability—behaving rather similarly to that of some noble-metal catalysts [11]. It was further suggested that the performance of this Sn/Cu nanocatalyst was sensitive to the amount of Sn deposited on the Cu electrode surface [12].

To date, many experimental [13–17] and theoretical [17–24] studies have been performed on this alloy system. However, a conclusive detailed picture of this rich surface-alloy phase diagram is still warranted. For less than a monolayer (ML) surface coverage of Sn on Cu(001), four different dominant surface phases have been suggested via scanning-tunneling-microscopy (STM) and low-energy-electron-diffraction (LEED) experiments: phases I–IV [15,16]. Namely, at approximately 0.2 ML of Sn, STM and LEED patterns suggest a phase-I structure which consists of an antiphase domain surface structure with a local $p(2 \times 2)$ surface periodicity coexisting with clean Cu(001), yielding a surface matrix notation of $\begin{pmatrix} 10 & 1 \\ 1 & 10 \end{pmatrix}$ [14,23,25]. Increasing the surface coverage of Sn to 0.333 ML, the coexistence of Sn/Cu(001) surface structures with periodicities of $p(6 \times 2)$ and $p(2 \times 2)$ has been identified and designated as phase II [13,15,24].

With Sn surface coverages of approximately 0.4 ML, Sn/Cu(001) surface structures with the notation of $\begin{pmatrix} -4 & 2 \\ 0 & 4 \end{pmatrix}$ have been reported and are eventually reconstructed to the $p(2 \times 2)$ structure upon annealing at higher temperatures [26,27]. Now, as half of a monolayer of Sn adatoms is deposited on Cu(001), LEED, STM, and surface x-ray-diffraction analyses seem to suggest the onset of phase III, i.e., ordered surface structures of $p(3\sqrt{2} \times \sqrt{2})R45^\circ$ and

*Corresponding author.
aloyus.soon@yonsei.ac.kr

$p(2\sqrt{2} \times 2\sqrt{2})R45^\circ$ simultaneously observed at 360 K [15,16,20,28]. This observation is sometimes followed by the transformation of the $p(2\sqrt{2} \times 2\sqrt{2})R45^\circ$ structure to $p(3\sqrt{2} \times \sqrt{2})R45^\circ$ or $c(4 \times 4)$ when the surface Sn coverage goes slightly beyond 0.5 ML [16,19–22].

Lastly, with increasing surface coverages of Sn from 0.5 ML to a full monolayer, new surface models have been proposed and suggested as likely structural candidates when compared to the known $c(4 \times 4)$ LEED patterns [22]. For example, the concurrence of phase III and a newer phase IV (which is suggested as phase III with additional Sn adatoms at approximately 0.63 ML of Sn) has been reported [17,22], but its definitive surface atomic structure and thermodynamic (meta)stability are clearly lacking.

Interestingly, the complexity of this Sn/Cu(001) surface system grows even more as one goes beyond the full-monolayer surface Sn coverage. Again, with STM and LEED data collected, yet another surface structure—phase V (which is a combination of the so-called phase D and phase T) has been suggested [16]. Starting with a Sn surface coverage of more than 0.625 ML, annealing the Sn/Cu(001) surface at 410 K generates a puzzling coexistence of phase III, phase D (“disordered” phase), and a periodic phase T [which has the surface notation $(\begin{smallmatrix} 4 & 3 \\ -3 & 4 \end{smallmatrix})$ and where the surface Sn coverage is speculated to reach as high as 2 ML]. Depending on the amount of Sn introduced to the surface, phase III may play a lesser role, while phase T dominates at higher Sn surface coverage [16].

In this work, through a systematic first-principles study of various chemisorbed, surface-substituted, and surface-alloy structures, we examine previous experimentally suggested Sn/Cu(001) phases (i.e., from phase I to phase IV) and discuss their relative thermodynamic stability within the *ab initio* thermodynamics framework as a function of the Sn surface coverage. The surface electronic structure of these low-energy Sn/Cu(001) surface structures is analyzed via their surface work functions and surface dipole moments with varying surface coverages of Sn. Our simulated STM images are then compared to experimentally available ones.

II. METHODOLOGY

All density-functional-theory (DFT) calculations are performed using the Vienna *ab initio* simulation package code [29,30]. We employ the projector-augmented-wave [31,32] method and the generalized-gradient approximation to the exchange-correlation functional due to Perdew, Burke, and Ernzerhof (PBE) [33]. The wave functions are expanded in a plane-wave basis set with a kinetic cutoff energy of 500 eV. The total energy differences and forces acting on each atom are converged to within 20 meV/atom and 0.02 eV/Å, respectively.

For the Brillouin-zone integrations, Monkhorst-Pack k -point grids of $(9 \times 9 \times 9)$ and $(6 \times 6 \times 6)$ are used for

bulk Cu ($Fm\bar{3}m$) and α -Sn ($Fd\bar{3}m$), respectively [34]. For the surface structures, the $(12 \times 12 \times 1)$ k -point grid is used for the Cu(001) $p(1 \times 1)$ surface and, thereafter, equivalent k -point density has been ensured for the larger surface cells (where the details are tabulated in the Supplemental Material [35]).

Asymmetric surface slab models containing four atomic layers of Cu are used while fixing the bottommost two layers to mimic bulk-atom positions and ensuring a vacuum region of approximately 18 Å. Here, adatoms of Sn atoms on Cu(001) are adsorbed on the surface of the slab where the common binding sites (bridge and hollow), surface or subsurface substitution, and several surface-alloy structures are considered for various surface monolayer coverages of Sn. Here, we define the surface coverage of Sn (Θ_{Sn}) as the ratio of the number of adsorbed Sn atoms to the number of atoms in an ideal Cu(001) $p(1 \times 1)$ substrate layer.

The average adsorption energy of Sn adatoms on Cu(001) as a function of its surface coverage, $E_{\text{ad}}^{\text{Sn}}$, is calculated as

$$E_{\text{ad}}^{\text{Sn}} = \frac{1}{N_{\text{Sn}}} (E_{\text{total}} - E_{\text{Cu}}^{\text{slab}} - N_{\text{Cu}}E_{\text{Cu}} - N_{\text{Sn}}E_{\text{Sn}}). \quad (1)$$

Here, E_{total} and $E_{\text{Cu}}^{\text{slab}}$ represent the total energy of Sn on Cu(001) and the clean surface of Cu(001), respectively. E_{Cu} , E_{Sn} , N_{Cu} , and N_{Sn} are then taken as the total energies of bulk α -Sn and Cu, and the total numbers of Sn adatoms and of excess Cu atoms, accordingly. A negative value here will indicate a thermodynamically stable (i.e., exothermic) adsorption structure.

Next, to compare the relative thermodynamic stability amongst the considered Sn/Cu(001) surface systems in this work, we proceed to calculate the change in the Gibbs free energy of adsorption, ΔG^{ad} , as a function of both chemical potential changes in Sn and Cu, using

$$\Delta G_{\text{ad}} \approx \frac{1}{A} (N_{\text{Sn}}E_{\text{ad}}^{\text{Sn}} - N_{\text{Sn}}\Delta\mu_{\text{Sn}} - N_{\text{Cu}}\Delta\mu_{\text{Cu}}), \quad (2)$$

where A and $E_{\text{ad}}^{\text{Sn}}$ [see Eq. (1)] are the surface area of the surface-slab model and the average adsorption energy of Sn adatoms on Cu(001), respectively. Accordingly, $\Delta\mu_{\text{Sn}}$ and $\Delta\mu_{\text{Cu}}$ are taken as the change of the atomic chemical potentials of Sn and Cu with respect to the standard reference states of bulk α -Sn and Cu, respectively. Here, we neglect other contributing terms (e.g., vibrational or configurational entropy) [8,36] to the calculated free energy of adsorption. Instead, we simply use an approximation of ± 0.1 eV to account for this possible uncertainty in the determination of $\Delta\mu_{\text{Cu}}$ (see Fig. 5).

To analyze and discuss the electronic structure of the Sn/Cu(001) systems, it is useful to define some quantities which we calculate and use in this work. We evaluate the surface work function (Φ) by taking the difference between

the electrostatic potential, U , in the middle of the vacuum region and the Fermi energy, ϵ_F , of the system (i.e., $\Phi = U - \epsilon_F$) [36,37]. The surface dipole moment (μ^{SD} in units of debye) is calculated using the Helmholtz equation

$$\frac{\Delta\Phi}{e} = \frac{\sigma\mu^{\text{SD}}}{\epsilon_0}, \quad (3)$$

where $\Delta\Phi$ is a change in the surface work function [taken with respect to the clean Cu(001) surface], σ is the surface atom density (Θ/A , where A is the unit surface area), and ϵ_0 is the vacuum permittivity. Here, we derive μ^{SD} [in debye (D)] as a function of Sn coverage (Θ_{Sn}),

$$\mu^{\text{SD}} = \frac{A\Delta\Phi}{12\pi\Theta_{\text{Sn}}}, \quad (4)$$

where A is taken to be the unit area of a $p(1 \times 1)$ surface unit of Cu(001), Θ_{Sn} is the surface monolayer coverage of Sn on Cu(001) [36,38]. Details of the derivation of Eq. (4) are provided in the Supplemental Material [35].

To examine the nature of bonding between the Sn adlayers on Cu(001), we calculate the difference electron density ($\Delta\rho$), where

$$\Delta\rho = \rho_{\text{Sn/Cu}} - \rho_{\text{Cu}} - \rho_{\text{Sn}}. \quad (5)$$

Here, $\rho_{\text{Sn/Cu}}$ is the total electron density of the Sn on a Cu(001) system from which the electron density of both clean Cu(001), ρ_{Cu} , and that of the isolated Sn adlayer, ρ_{Sn} , are subtracted, while we restrict their respective atomic positions to those of the corresponding geometry-relaxed system. We also further compare the planar-averaged difference electron densities [$\Delta\rho_{\text{ave}}(z)$, projected in one dimension along the z axis] to rationalize the trends for both $\Delta\Phi(\Theta_{\text{Sn}})$ and $\mu^{\text{SD}}(\Theta_{\text{Sn}})$.

In addition, we employ the Tersoff-Hamann approach [39], as implemented in the HIVE code [40], to simulate and visualize the STM images of Sn on Cu(001). Here, to mimic the applied bias voltage in experiments, we perform the integration of the local density of states to obtain the partial charge densities, within an energy window of 0.5 eV below the Fermi level to the Fermi level, while keeping a constant height of 2.5 Å above the surface.

III. RESULTS AND DISCUSSION

A. Bulk Cu, α -Sn, β -Sn, and Sn_xCu_y alloys

The calculated bulk properties of bulk Cu, α -Sn, and β -Sn are close to the previously reported theoretical and experimental values. For bulk Cu, our calculated lattice constant, a_0 , is 3.64 Å, agreeing well with the established theoretical and experimental values of 3.64 and 3.61 Å, respectively [41–43].

For bulk Sn, the various allotropic phases of Sn are considered, and we fit our calculated PBE energy-volume

curves to the third-order Birch-Murnaghan equation of state (Fig. S2 of the Supplemental Material [35]). For the most stable α -Sn, the calculated a_0 value is 6.65 Å, while the next most stable β -Sn, a_0 , is found to be 5.99 Å with a c/a ratio of 0.53. These calculated values for both α -Sn and β -Sn agree well with the available experimental findings, namely, $a_{\text{Sn}} = 6.49$ Å for α -Sn [44], and 5.83 Å and 0.55 for a_0 and the c/a ratio of β -Sn [45], respectively. The reported theoretical values for a_0 for α -Sn and β -Sn are 6.65 and 5.97 Å, respectively, with the c/a ratio of β -Sn being 0.53 [46] (See Table S1 of the Supplemental Material [35] and Refs. [44,45,47–52]).

In addition, the lattice parameters of various Sn_xCu_y alloys are considered and optimized. Their relative thermodynamic stability, with the hexagonal SnCu (h -SnCu) being the most stable phase at 50:50 composition, is reported in Fig. S1 of the Supplemental Material [35].

B. Surface structures of Sn/Cu(001)

The adsorption of Sn on Cu(001) is known to result in a variety of surface structures, ranging from simple chemisorption phases to complex surface alloys, as reported in previous literature [13–17,21,22,24]. Using surface characterization techniques like LEED and STM, and also from earlier DFT studies, various authors have proposed Sn/Cu(001) surface structures that may be broadly classified into three main categories: simple chemisorption [Fig. 1(a)], surface substitution [Fig. 1(b)], and surface alloys [Fig. 1(c)].

1. Chemisorption and surface substitution

As shown in Fig. 1(a), we consider the fourfold hollow (H) and twofold bridge (B) sites at various surface coverages of Sn on Cu(001) ranging from 0.125 to 1.0 ML. The on-top site is not found to be favorable. For the family of surface-substituted (S) structures, we generate 13 S models at various surface coverages of Sn, as depicted in Fig. 2. As inspired by some structures reported in previous literature [13,14,16,17,19,21,24], selected surface Cu atoms are replaced by Sn atoms, yielding surface coverages of Sn from 0.125 to 0.6 ML.

More specifically, an antiphase domain structure—phase I [14,23,27] with a local $p(2 \times 2)$ surface periodicity—is identified. Here, to model this phase I, we construct a fairly large surface structure, with a matrix notation of $\begin{pmatrix} 10 & 1 \\ 1 & 10 \end{pmatrix}$ and a total of almost 400 atoms in this model [Fig. 2(b)]. We also consider other possible local $p(2 \times 2)$ surface periodic models such as those shown in Figs. 2(d) (with $\Theta_{\text{Sn}} = 0.25$ ML) and 2(l) (with $\Theta_{\text{Sn}} = 0.5$ ML).

Another commonly reported phase, phase II [16] is modeled using a $p(6 \times 2)$ surface cell. However, it is known that phase II may coexist with the $p(2 \times 2)$ phase [15] or the $\begin{pmatrix} -4 & 2 \\ 0 & 4 \end{pmatrix}$ structure (with $\Theta_{\text{Sn}} = 0.375$ ML) [15,17,27], as shown in Fig. 2(g). In Fig. 2(j), another

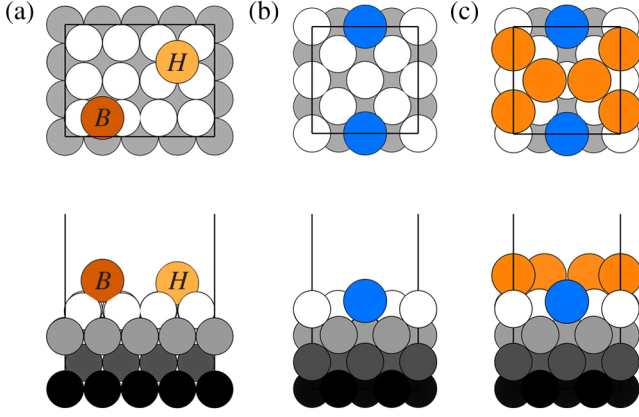


FIG. 1. Top and side views of the atomic surface structures of Sn/Cu(001) systems. (a) Simple chemisorption of Sn adatoms at the bridge (labeled B , shown in darker orange) and the hollow (labeled H , shown in lighter orange) sites on the Cu(001) surface. (b) Surface-substituted Sn adatoms (shown in blue) in the outermost Cu layer. This group of surface structures is labeled S in the text. (c) Complex surface-alloy formation via a mixture or combination of additional Sn adatoms or adlayers (shown in orange) and surface-substituted Sn atoms (shown in blue) on top of the Cu(001) surface, and they are denoted as SA surface structures in the text. The Cu(001) surface atoms are shaded from black to white, with the innermost bulklike atoms in black.

frequently observed Sn/Cu(001) surface phase (phase III) [13,16,17,19,21] is constructed with a surface supercell $p(3\sqrt{2} \times \sqrt{2})R45^\circ$. For comparison, we also generate a smaller $p(\sqrt{2} \times \sqrt{2})R45^\circ$ supercell [in Fig. 2(k)] where the missing-row reconstruction in phase III is lifted.

2. Surface alloys

A total of 14 Sn/Cu surface alloys (SAs) are considered in this work and these SA surface models yield Sn surface coverages ranging from 0.333 to 1.0 ML (See Fig. 3). Many of these SA surface models have been derived from reported experiments and earlier theoretical studies [17,22,24]. A newer phase V has been suggested, but a severe lack of atomic details hinders the overall comprehension of this alloy system.

Namely, a higher-surface-coverage (i.e., $\gtrsim 0.6$ ML) Sn/Cu(001) phase—phase IV [16,22]—has been suggested and is represented by a surface supercell $c(4 \times 4)$ in this work. As guided by STM and LEED simulation data [16,22], various possible configurations for this phase are constructed and depicted in Figs. 3(b)–3(g), 3(j)–3(l), and 3(n). We note that phase IV has been reported to coexist with phase III.

C. Surface energetics and thermodynamics of Sn/Cu(001)

1. Adsorption energetics

Using Eq. (1), we calculate the average adsorption energy, $E_{\text{ad}}^{\text{Sn}}$, of Sn adatoms on Cu(001) as a function

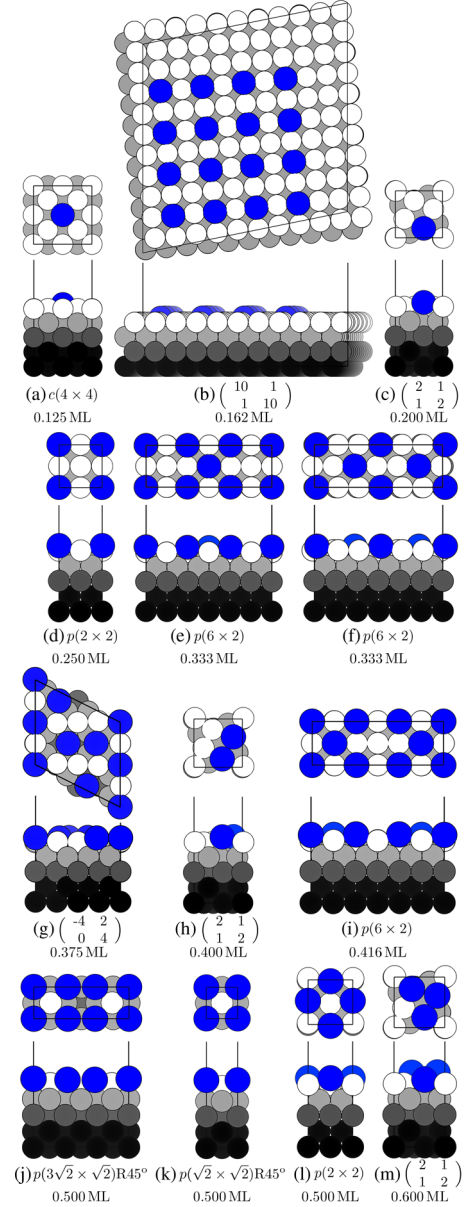


FIG. 2. The S family of surface-substituted Sn/Cu(001) surface structures [see Fig. 1(b) for the atom color scheme]. Here, both the top and side views of the optimized atomic surface structures are shown, with the corresponding Θ_{Sn} value listed below each structure. Specifically, for the following S surface structures, we adapt their surface geometries from previous literature: (b) from Refs. [13,14], (d) from Refs. [14,23], (e) from Ref. [17], (f) from Refs. [17,24], (g) from Ref. [27], (i) from Ref. [17], and (j) from Refs. [13,16,17,19,21]. All other surface structures are newly constructed for comparison and discussion in the main text.

of its surface coverage, Θ_{Sn} , presented in Fig. 4. Here, $E_{\text{ad}}^{\text{Sn}}$ is computed with respect to the total energy of bulk α -Sn, and their numerical values (-0.93 to 0.90 eV) are tabulated in Tables S2–S4 of the Supplemental Material [35].

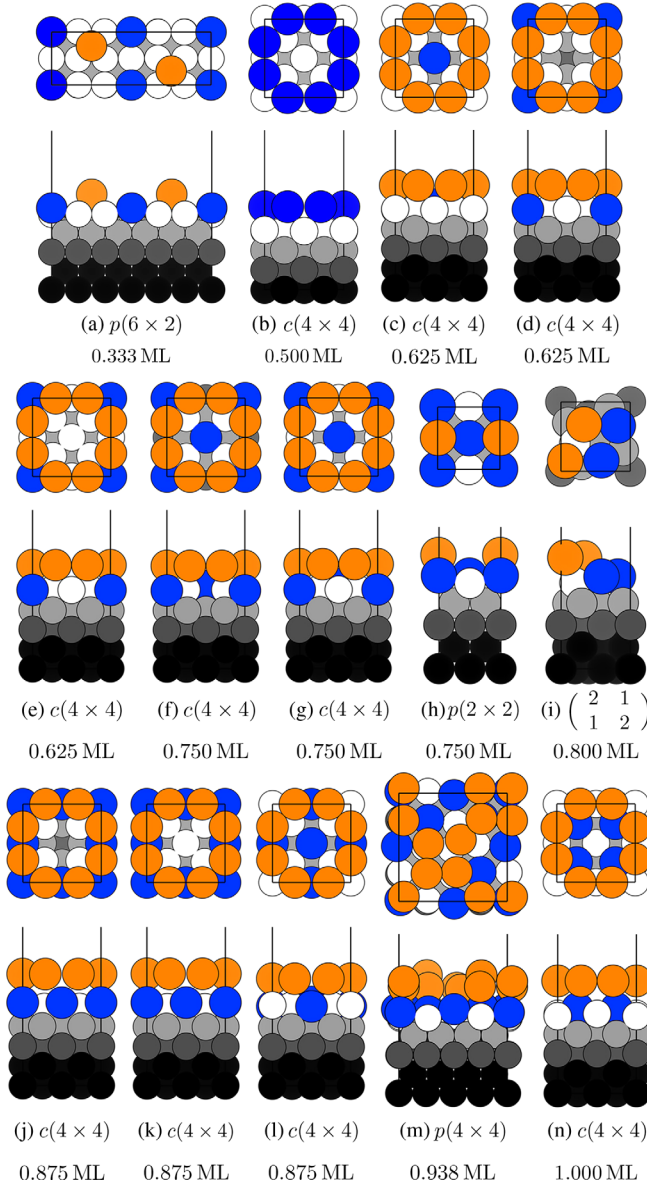


FIG. 3. The SA family of surface-substituted Sn/Cu(001) surface structures [see Fig. 1(c) for the atom color scheme]. Here, both the top and side views of the optimized atomic surface structures are shown, with the corresponding Θ_{Sn} value listed below each structure. Specifically, for the following SA surface structures, we adapt their surface geometries from previous literature: (a) from Refs. [17,24], and (b)–(g) and (j)–(n) from Ref. [22]. All other surface structures are newly constructed for comparison and discussion in the main text.

However, if one were to compute $E_{\text{ad}}^{\text{Sn}}$ with respect to the atomic state of Sn (note that the cohesive energy of bulk α -Sn is calculated to be -3.18 eV), the calculated values for $E_{\text{ad}}^{\text{Sn}}$ now span over a range of -4.11 to -2.29 eV. These values will ease our discussion when comparing the adsorption energies reported for other bimetallic adsorbate-substrate systems: from -3.8 to -2.7 eV for Co/Cu(001) [53], -4.1 to -2.9 eV for Sb/Cu(001)

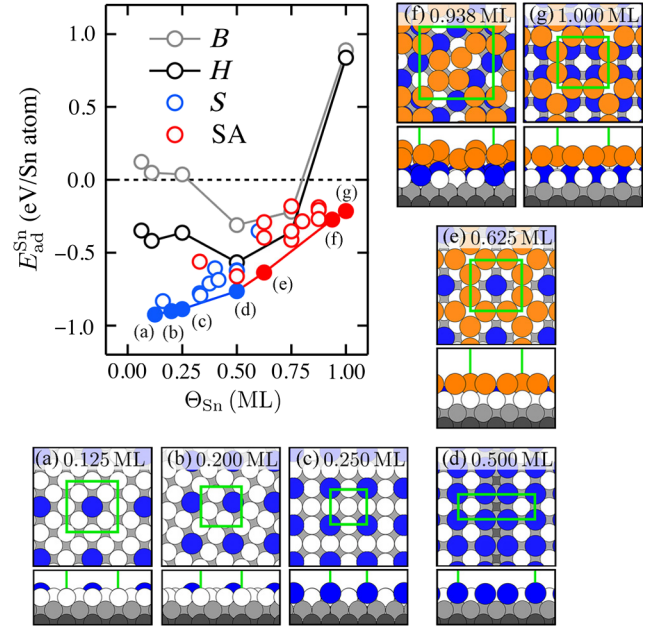


FIG. 4. Calculated average adsorption energy, $E_{\text{ad}}^{\text{Sn}}$, of Sn adatoms on Cu(001) as a function of its surface coverage, Θ_{Sn} , with respect to the energy of bulk α -Sn [see Eq. (1)]. The average adsorption-energy values for Sn chemisorbed at the bridge (B) and hollow (H) sites are shown as gray and black open circles, respectively, while those for the S and SA structures are shown as blue and red open circles. For those structures with the most negative $E_{\text{ad}}^{\text{Sn}}$ values, they are represented by the corresponding filled (blue or red) circle and connected by solid lines to aid viewing. Atomic details of these low-energy surface structures are also shown as inserts (a)–(g), respectively (see Fig. 1 for the atom color scheme).

[54], -4.7 to -3.7 eV for Sn/Ni(001) [55], and -4.5 to -3.4 eV for Sn/Au(111) [56].

Comparing the surface structures within the $p(6 \times 2)$ family, i.e., for S and SA structures with $\Theta_{\text{Sn}} = 0.333$ and 0.416 ML [see Figs. 2(e), 2(f), 2(i), and 3(a)], we find that the SA Sn/Cu(001) surface structure with a less coordinated Sn atom [Fig. 3(a)] has a less exothermic adsorption energy (-0.562 eV). This value is in contrast to former S surface structures [shown in Figs. 2(e), 2(f), and 2(i)] where a more favorable adsorption energy is obtained (i.e., -0.778 , -0.793 , and -0.778 eV, respectively).

Upon increasing Θ_{Sn} to 0.5 ML, we observe a more negative adsorption energy amongst the chemisorption phases (both B and H) at this surface coverage. Also, at $\Theta_{\text{Sn}} = 0.5$ ML, the missing-row reconstruction for the S structure is deemed the most stable [$p(3\sqrt{2} \times \sqrt{2})R45^\circ$ with $E_{\text{ad}}^{\text{Sn}} = -0.764$ eV; see Figs. 2(j) and 4(d)] when compared to the one without [$p(\sqrt{2} \times \sqrt{2})R45^\circ$ with $E_{\text{ad}}^{\text{Sn}} = -0.621$ eV; see Fig. 2(k)]. In the former, surface relaxation is encouraged so as to accommodate the larger-sized Sn adatoms and displacing the Sn adatoms near the missing row to a smaller Sn-Sn distance (from 3.636 to 3.124 Å). This adsorbate-induced reconstruction involves

the neighboring Cu atoms, and a strong electronic coupling is found via the difference-electron-density plots (which are addressed below; see Fig. 8).

When $0.5 < \Theta_{\text{Sn}} \leq 1.0$ ML, we find a general repulsive adsorption behavior for most Sn/Cu(001) surface structures. This behavior is especially obvious when one inspects the adsorption values for the chemisorption H and B series. Taking the full monolayer coverage (i.e., $\theta_{\text{Sn}} = 1.0$ ML) as an extreme example where the value of $E_{\text{ad}}^{\text{Sn}}$ becomes positive, the Sn-Sn distance is measured to be 2.57 Å, which is shorter than that normally found in bulk Sn (3.10 Å in β -Sn and 2.88 Å in α -Sn). On the flip side, in the case where the substrate has a larger lattice constant than Cu, this Sn-Sn repulsive behavior is not found. For instance, in the Sn/Au(111) system [56], this Sn-Sn repulsion is reported to be greatly minimized on Au(111) at higher surface coverages of Sn.

Besides taking the size and distance of Sn into account, we also find a strong correlation between the number of neighboring atoms (i.e., the effective coordination number) of Sn and its adsorption strength. This correlation is more apparent for the S and SA family of surface structures where the substituted Sn atom with the highest effective coordination number (a maximum of eight neighbors) shows the most exothermic $E_{\text{ad}}^{\text{Sn}}$. This dependence has also been observed for other bimetallic adsorbate-substrate systems [53,56], where the effective coordination number of the substituted adsorbate is known to influence its bonding strength significantly. This correlation has been rationalized by the up-shifting and broadening of the adatom's electronic bands, favoring a strong substitutional-adsorption process.

For example, in the case of Co/Cu(001), the valence 3d bands of the substituted Co are reported to be more broad and shifted towards the Fermi level, relating to a stronger bonding at the substitutional geometry [53]. For specific cases where the difference in electronegativity between the adsorbate and the substrate is very high [e.g., in the O/Cu(001) [37] and N/Cu(001) systems [57]], a more drastic shift may be expected.

Collectively, from Fig. 4, we clearly show that simple chemisorption phases (both H and B , indicated by black and gray markers, respectively) are less favorable than the S and SA Sn/Cu surface structures (which are denoted by blue and red markers, respectively). This finding corroborates well with the experimental findings that Sn-substituted structures are preferred to on-surface chemisorption on Cu surfaces [53,54,58–61]. Referring to Fig. 4, we aid the discussion of the preferred adsorption structures by considering those structures with the lowest $E_{\text{ad}}^{\text{Sn}}$ connected with solid blue or red lines, and we proceed to examine their relative thermodynamic stability as a function of the constituent atomic chemical potentials.

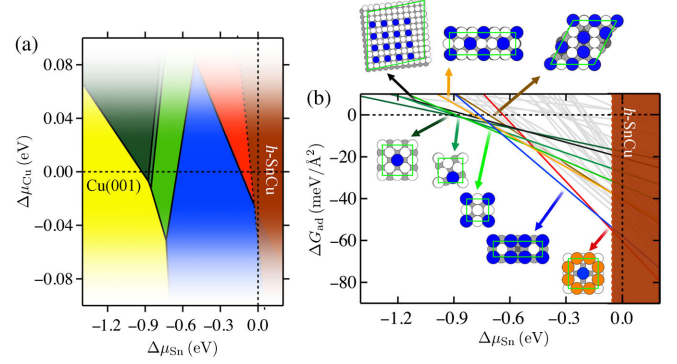


FIG. 5. (a) Calculated Gibbs free energy of Sn adsorption on Cu(001), ΔG_{ad} , as a function of the change in both the Sn and Cu chemical potentials (i.e., $\Delta\mu_i = \mu_i - \mu_i^{\text{ref}}$, where i represents Sn or Cu and their elemental bulk energies are taken as the reference states). Considering possible uncertainty (e.g., from temperature or entropic effects) in the theoretically well-defined (but appropriate) reference states for both Sn and Cu, the dependence of ΔG_{ad} outside these reference limits is also plotted (and made hazy). Specifically, for $\Delta\mu_{\text{Cu}}$, an uncertainty of approximately ± 0.1 eV is assumed. (b) ΔG_{ad} with varying Sn chemical potentials, $\Delta\mu_{\text{Sn}}$ (taking $\Delta\mu_{\text{Cu}} = 0$ eV). For both plots, regions of stability are color coded, with the corresponding surface structure (the top view) illustrated nearby: Olive, green, lime, blue, and red lines (or planes) represent $c(4 \times 4)$ -0.125 ML [see Fig. 2(a)], $\begin{pmatrix} 2 & 1 \\ 1 & 2 \end{pmatrix}$ -0.2 ML [see Fig. 2(c)], $p(2 \times 2)$ -0.25 ML [see Fig. 2(d)], $p(3\sqrt{2} \times \sqrt{2})R45^\circ$ -0.5 ML [see Fig. 2(j)], and $c(4 \times 4)$ -0.625 ML [see Fig. 3(c)], respectively. Other metastable structures are color coded in (b): Black, orange, and brown lines represent $\begin{pmatrix} 10 & 1 \\ 1 & 10 \end{pmatrix}$ -0.162 ML [see Fig. 2(b)], $p(6 \times 2)$ -0.333 ML [see Fig. 2(f)], and $\begin{pmatrix} -4 & 2 \\ 0 & 4 \end{pmatrix}$ -0.375 ML [see Fig. 2(g)], respectively. The bulk h -SnCu alloy formation is then depicted by the dark-brown shaded regions.

2. Thermodynamic surface phase diagram

Using Eq. (2) with the *ab initio* atomistic thermodynamics framework [8,38,62–64], we calculate the Gibbs free energy of adsorption of Sn on Cu(001), ΔG_{ad} , as a function of the change in both the Sn and Cu chemical potentials ($\Delta\mu_{\text{Sn}}$ and $\Delta\mu_{\text{Cu}}$, respectively). We define this change in the atomic chemical potential with respect to the ground-state bulk metal, i.e., bulk Cu and bulk α -Sn, accordingly. The result is presented in Fig. 5, where vibrational and configurational entropy terms are first neglected.

To account for possible uncertainty (e.g., from temperature or entropic effects, etc.) in the theoretically well-defined (but appropriate) reference bulk states for both Sn and Cu, the dependence of ΔG_{ad} outside these reference limits is also considered. Specifically, for $\Delta\mu_{\text{Cu}}$, an uncertainty of approximately ± 0.1 eV is assumed [as indicated by the hazy region in Fig. 5(a)]. We find that the overall conclusions drawn in this work are not greatly affected by the uncertainty in the reference limits. For instance, if $\Delta\mu_{\text{Cu}}$ happens to take a slightly positive value, the

predicted phases $c(4 \times 4)$ -0.125 ML (shown in olive) and $c(4 \times 4)$ -0.625 ML (shown in red) will occupy only a slightly larger area in the stability phase space.

Thus, we focus our discussion on the overall surface thermodynamics of Sn/Cu(001) where $\Delta\mu_{\text{Cu}}$ is taken to be an absolute 0 eV [Fig. 5(b)]. For very low values of $\Delta\mu_{\text{Sn}}$, the clean Cu(001) surface is the most stable. With increasing Sn content on the Cu(001) surface, we find that the $c(4 \times 4)$ -0.125 ML and $\begin{pmatrix} 2 & 1 \\ 1 & 2 \end{pmatrix}$ -0.2 ML surface structures are marginally stable, before the onset of $p(2 \times 2)$ -0.25 ML with a slightly wider energy window of stability. Next, the $p(3\sqrt{2} \times \sqrt{2})R45^\circ$ -0.5 ML surface structure dominates for much higher values of $\Delta\mu_{\text{Sn}}$, followed by $c(4 \times 4)$ -0.625 ML before the formation of bulk h -SnCu commences.

Within the accuracy of our calculations, we deem structures predicted at lower values of $\Delta\mu_{\text{Sn}}$ to be almost degenerate (i.e., showing minimal energy differences). This argument may also extend to the DFT-predicted metastable structures: $\begin{pmatrix} 10 & 1 \\ 1 & 10 \end{pmatrix}$ -0.162 ML [the black line in Fig. 5(b)] and $p(6 \times 2)$ -0.333 ML [the orange line in Fig. 5(b)]. As discussed in our previous study of metastable O/Cu(111) surfaces [64], coexistence of almost degenerate (meta)stable structures may well be possible for the Sn/Cu(001) system, supporting the observation of phase I [with a local $p(2 \times 2)$ surface periodicity] [14,23,27] and phase II [16].

For higher values of $\Delta\mu_{\text{Sn}}$, the predicted stable surface structure is $p(3\sqrt{2} \times \sqrt{2})R45^\circ$ -0.5 ML, agreeing well with the experimental observation of phase III [17,22]. We argue that if the formation of bulk h -SnCu alloy is kinetically hindered in experiments, the energy window of stability for the experimentally suggested phase IV [16,22], $c(4 \times 4)$ -0.625 ML may be enlarged. To date, the formation of the bulk-alloy phase on Sn/Cu(001) has not been reported in experiments.

D. Surface electronic structure of Sn/Cu(001)

1. Work functions and surface dipole moments

Now, turning to the electronic structure of these Sn/Cu(001) surface structures, we first examine the calculated surface work functions and surface dipole moments with varying Θ_{Sn} 's [using Eq. (4)], as shown in Fig. 6 and listed in Tables S2–S4 in the Supplemental Material [35]. With increasing values of Θ_{Sn} up to 1.0 ML, the surface work function of Sn/Cu(001) generally show a decreasing trend when compared to that of pristine Cu(001). The work function of the pristine Cu(001) surface is calculated to be 4.48 eV, and the largest change in the work function (0.78 eV) is observed for the 1-ML surface coverage of Sn at the H site. Here, the change in the magnitude of the surface work function is considerably less than in the cases of alkali-metal adsorption [65], but of similar magnitude for other transition-metal adsorbates [53].

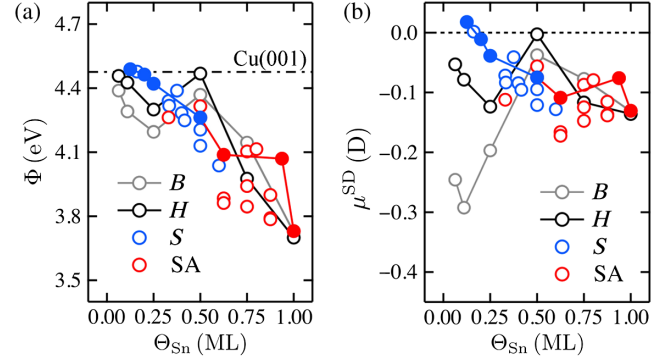


FIG. 6. Calculated (a) work function, Φ , and (b) surface dipole moment, μ^{SD} [in debye (D); see Eq. (4)], as a function of the surface coverage of Sn, Θ_{Sn} . The work function of the pristine Cu(001) surface is calculated to be 4.48 eV, and it is indicated by the dotted-dashed line in (a). Values for Sn chemisorbed at the bridge (B) and hollow (H) sites are shown as gray and black open circles, respectively, while those for the S and SA structures are shown as blue and red open circles. Filled (blue and red) circles connected by solid lines represent the most energetically stable S and SA structures, and they serve as a guide for the eye.

More specifically, in comparison to the trends seen for the B and H chemisorption phases of Sn/Cu(001) in this work, a rather similar *inverted-parabola* behavior is reported for Co/Cu(001) (up to 0.5 ML). Beyond half a monolayer, we find a monotonic decrease in the work function for Sn/Cu(001), while the opposite is found for the Co/Cu(001) system [53]. This observation seems to correlate well with our calculated $E_{\text{ad}}^{\text{Sn}}$ value (in Fig. 4), as rationalized via the highly compressed Sn adatoms in the lateral direction for very high surface coverages.

With this correlation noted, it has been further indicated that a reduction in the surface dipole moment for a highly compressed metal adlayer could be a natural consequence of lowering the repulsive interaction between the metal adatoms [53]. From our study [see Fig. 6(b)], we find that the Helmholtz relation (i.e., $\mu^{\text{SD}} \propto \Delta\Phi/\Theta$) between the change in the surface work function and the calculated surface dipole moment for the Sn/Cu(001) system is obeyed. The observed decrease in the surface work function with increasing Θ_{Sn} can be explained in terms of the formation of a small inward-pointing surface dipole moment (i.e., ≤ 0.3 D in magnitude, noting that the difference in electronegativity between Sn and Cu is very marginal). The highly compressed Sn adlayer in the chemisorption phases at higher surface Sn coverages then encounters a competition between surface depolarization and surface stress or tension due to very short Sn-Sn bond distances. Unlike the chemisorption phases, the S and SA family of Sn/Cu(001) structures benefit from large surface relaxations and reconstructions to relieve the compression,

TABLE I. List of the averaged adsorption energy of Sn, $E_{\text{ad}}^{\text{Sn}}$ [see Eq. (1)]; work function, Φ ; and surface dipole moment, μ^{SD} [see Eq. (4)], for various low-energy Sn/Cu(001) surface structures at the corresponding Sn surface coverage, Θ_{Sn} . The work function of pristine Cu(001) is calculated to be 4.48 eV.

	Surface structure	Θ_{Sn} (ML)	$E_{\text{ad}}^{\text{Sn}}$ (eV/Sn atom)	Φ (eV)	μ^{SD} (D)
Fig. 2(a)	$c(4 \times 4)$	0.125	-0.925	4.49	0.02
Fig. 2(c)	$\begin{pmatrix} 2 & 1 \\ 1 & 2 \end{pmatrix}$	0.2	-0.901	4.46	-0.01
Fig. 2(d)	$p(2 \times 2)$	0.25	-0.887	4.42	-0.04
Fig. 2(f)	$p(6 \times 2)$	0.333	-0.793	4.32	-0.08
Fig. 2(j)	$p(3\sqrt{2} \times \sqrt{2})R45^\circ$	0.5	-0.764	4.26	-0.07
Fig. 3(c)	$c(4 \times 4)$	0.625	-0.636	4.09	-0.11

as reflected in the moderate variations in the surface dipole moments with Θ_{Sn} . The corresponding values of $E_{\text{ad}}^{\text{Sn}}$, Φ , and μ^{SD} for the low-energy Sn/Cu(001) surface structures are tabulated in Table I.

2. Electron density differences

The surface dipole moment of adsorbate or adlayer moment is a direct consequence of the redistribution of surface electron density upon adsorption [36]. To gain further insight into the surface electronic structure of Sn/Cu(001), we examine the difference-electron-density plots, $\Delta\rho$ [see Eq. (5)], for some low-energy surface structures, as shown in Fig. 7. The corresponding planar-averaged $\Delta\rho_{\text{ave}}(z)$ as projected along the z axis is also depicted.

Here, we choose to compare the electron density reorganization for the low-energy surface structures with the smallest work function change, i.e., $c(4 \times 4)$ -0.125 ML [Fig. 7(a)] and $p(2 \times 2)$ -0.25 ML [Fig. 7(b)], versus those

with the largest (albeit still small in terms of the magnitude) change in work function: $p(3\sqrt{2} \times \sqrt{2})R45^\circ$ -0.5 ML [Fig. 7(c)] and $c(4 \times 4)$ -0.625 ML [Fig. 7(d)].

From Fig. 7, at first glance, we measure a relatively larger change in the electron density redistributions for structures with a higher work function change than those with a smaller variation. As discussed above, this redistribution lends support to the close correlation between the work-function changes and a small negative surface dipole moment induced by the electron density redistribution between the Sn and Cu atoms, as inferred from the integration

of the $\Delta\rho_{\text{ave}}(z)$ graphs. Both $c(4 \times 4)$ -0.125 ML and $p(2 \times 2)$ -0.25 ML (with $\Delta\Phi = 0.01$ and -0.01 eV, respectively) show an almost negligible electron accumulation towards the Sn atoms, while $p(3\sqrt{2} \times \sqrt{2})R45^\circ$ -0.5 ML and $c(4 \times 4)$ -0.625 ML (with $\Delta\Phi = -0.22$ and -0.62 eV, respectively) display a much larger electron depletion in the outermost Sn atoms. The examination of

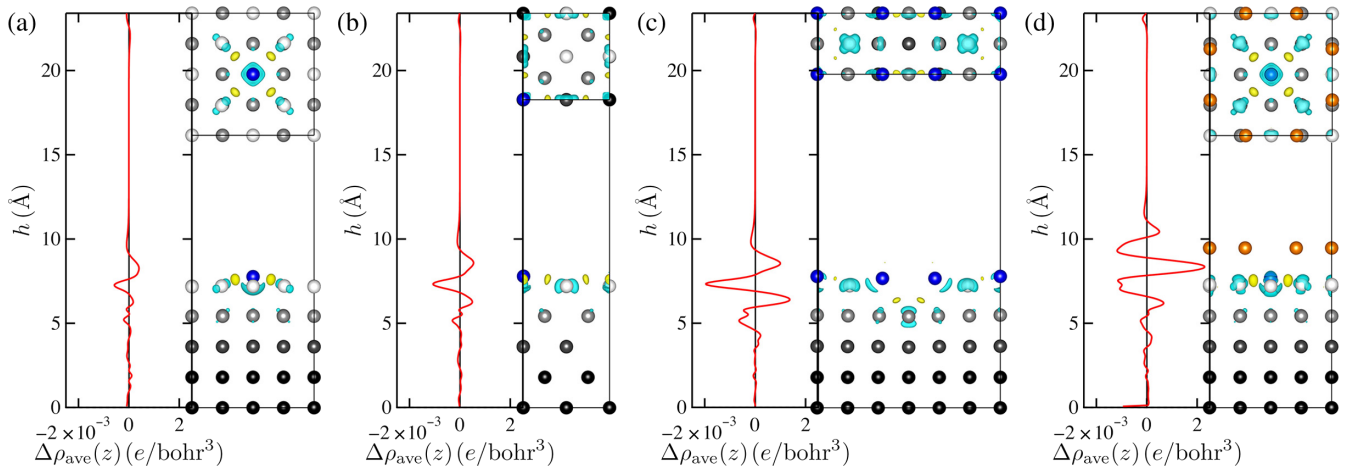


FIG. 7. Difference-electron-density plot [$\Delta\rho$; see Eq. (5), right-hand side] and the planar-averaged $\Delta\rho_{\text{ave}}(z)$ value as projected along the z axis (left) for (a) $c(4 \times 4)$ -0.125 ML [see Fig. 2(a)], (b) $p(2 \times 2)$ -0.25 ML [see Fig. 2(d)], (c) $p(3\sqrt{2} \times \sqrt{2})R45^\circ$ -0.5 ML [see Fig. 2(j)], and (d) $c(4 \times 4)$ -0.625 ML [see Fig. 2(d)]. Here, the atom coloring scheme follows Fig. 1. The isosurface level used is $\pm 0.001 e/\text{bohr}^3$, and the accumulation and the depletion of electron densities are indicated by the yellow and light-blue regions, respectively.

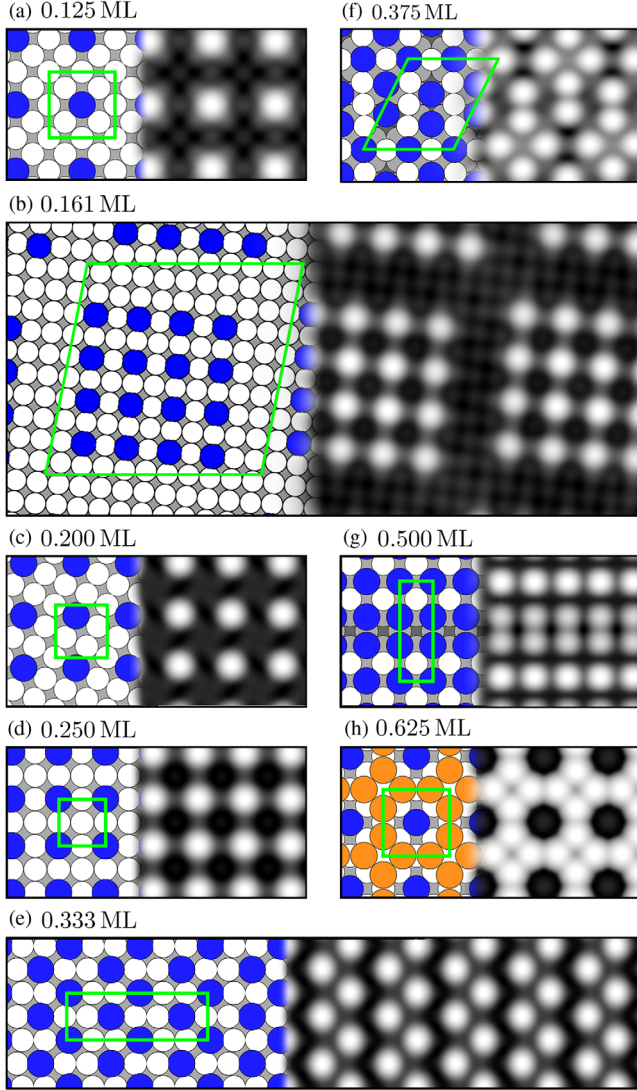


FIG. 8. DFT-derived simulated Tersoff-Hamann STM images (with the corresponding top view of the atomic structures) of (a) $c(4 \times 4)$ -0.125 ML [see Fig. 2(a)], (b) $\begin{pmatrix} 10 & 1 \\ 1 & 10 \end{pmatrix}$ -0.162 ML [phase I; see Fig. 2(b)], (c) $\begin{pmatrix} 2 & 1 \\ 1 & 2 \end{pmatrix}$ -0.2 ML [see Fig. 2(c)], (d) $p(2 \times 2)$ -0.25 ML [see Fig. 2(d)], (e) $p(6 \times 2)$ -0.333 ML [Fig. 2(f)], (f) $\begin{pmatrix} -4 & 2 \\ 0 & 4 \end{pmatrix}$ -0.375 ML [phase II; see Fig. 2(g)], (g) $p(3\sqrt{2} \times \sqrt{2})R45^\circ$ -0.5 ML [phase III; see Fig. 2(j)], and (h) $c(4 \times 4)$ -0.625 ML [phase IV; see Fig. 3(c)]. Here, the atom coloring scheme follows Fig. 1. For each Sn/Cu(001) surface structure, the surface unit cell is shown as lime-green lines. A more detailed comparison with the experimental STM images can be found in Fig. S3 of the Supplemental Material [35].

the difference-electron-density plots corroborates well with our calculated surface work-function and dipole-moment trend studies.

3. Scanning tunneling microscopy

To reconcile our first-principles-calculated atomic- and electronic-structure results with previous experiments

(namely, STM measurements [15,17,22,27]), we calculate and generate the DFT-derived simulated Tersoff-Hamann STM images for the occupied states by integrating the local density of states from 0.5 eV below the Fermi energy to the Fermi level. Within the constant-mode approach (of approximately 2.5 Å above the surface), we present the simulated STM images for the $c(4 \times 4)$ -0.125 ML, $\begin{pmatrix} 10 & 1 \\ 1 & 10 \end{pmatrix}$ -0.162 ML (phase I), $\begin{pmatrix} 2 & 1 \\ 1 & 2 \end{pmatrix}$ -0.2 ML, $p(2 \times 2)$ -0.25 ML, $p(6 \times 2)$ -0.333 ML, $\begin{pmatrix} -4 & 2 \\ 0 & 4 \end{pmatrix}$ -0.375 ML (phase II), $p(3\sqrt{2} \times \sqrt{2})R45^\circ$ -0.5 ML (phase III), and $c(4 \times 4)$ -0.625 ML (phase IV) in Fig. 8.

Overall, the simulated STM images of our DFT predicted stable and metastable Sn/Cu(001) values agree very well with previous experimental STM reports (with the detailed STM comparison between experiments and our theoretical results shown in Fig. S3 of the Supplemental Material [35]). The bright spots are identified as the outermost Sn atoms [the blue Sn atoms in Figs. 8(a)–8(g) and the orange Sn atoms in Fig. 8(h)], while the strong contrast in the dark regions reflects the substrate Cu atoms or surface vacancies. We rationalize this finding by referring to the projected density of states of, e.g., $c(4 \times 4)$ -0.125 ML, as shown in Fig. S4 of the Supplemental Material [35], where the dominance of occupied $5p$ states of Sn below the Fermi level is demonstrated.

IV. CONCLUSION

In this work, we examine the rich variety of Sn/Cu(001) surface structures and have calculated the surface energetics and thermodynamics of this system as a function of the surface coverage of Sn, identifying the low-energy structures for phases I–IV, as speculated from experimental STM measurements. Our results indeed show that, at low Sn surface coverages (or lower chemical potentials of Sn), many energetically competitive surface structures are identified. They contain local $p(2 \times 2)$ surface motifs in phase I and the $p(6 \times 2)$ motif in phase II, as correctly suggested by experimental STM images. Moving to higher Sn surface coverages, the dominant surface structure is $p(3\sqrt{2} \times \sqrt{2})R45^\circ$ and is assigned to phase III, while the $c(4 \times 4)$ structure is designated as phase IV.

The surface electronic structure is analyzed via the computed surface work functions and dipole moments with varying Sn surface coverage. In comparison to other bimetallic adsorbate-substrate systems like Co/Cu(001), we find a complex mechanism of electron transfer between the Sn adlayers and Cu(001) where, especially at higher surface coverages of Sn, repulsive lateral interactions between the highly compressed Sn adatoms in the chemisorption phases invert the trends. Surface alloys and surface-substitution Sn/Cu(001) structures relieve this compressive interaction via strong surface relaxations and reconstructions. To reconcile our DFT-identified Sn/Cu(001) structures with the various experimentally observed phases I–IV,

our DFT-derived simulated Tersoff-Hamann STM images of these low-energy structures concur very well with experimental STM measurements.

With a better understanding of the complex surface phase diagram of Sn/Cu(001), we now have a more complete picture of possible Sn/Cu surface structures for different Sn compositions. This provides a good basis for future studies in surface-sensitive applications (e.g., in selective CO₂ reduction and surface self-assembly mechanisms), where the surface electronic structure of this alloy system will come in handy.

ACKNOWLEDGMENTS

We gratefully acknowledge the support from the National Research and Development Program of Ministry of Science, ICT and Future Planning (Project No. 2017M3A7B4032124). Computational resources have been kindly provided by the KISTI Supercomputing Center (Grant No. KSC-2017-C3-0008) and the Australian National Computational Infrastructure (NCI). We thank Dr. L. O. Paz-Borbón for the helpful discussions regarding this work.

J.-H. L. and J. Y. contributed equally to this work.

-
- [1] S. D. Beattie and J. R. Dahn, Single bath, pulsed electro-deposition of copper-tin alloy negative electrodes for lithium-ion batteries, *J. Electrochem. Soc.* **150**, A894 (2003).
- [2] M. Xue, W. Wang, F. Wang, J. Ou, C. Li, and Wen Li, Understanding of the correlation between work function and surface morphology of metals and alloys, *J. Alloys Compd.* **577**, 1 (2013).
- [3] A. Carrera, L. J. Cristina, S. Bengió, A. Cossaro, A. Verdini, L. Floreano, J. D. Fuhr, J. E. Gayone, and H. Ascolani, Controlling carboxyl deprotonation on Cu(001) by surface Sn alloying, *J. Phys. Chem. C* **117**, 17058 (2013).
- [4] N. D. Orf, I. D. Baikie, O. Shapira, and Y. Fink, Work function engineering in low-temperature metals, *Appl. Phys. Lett.* **94**, 113504 (2009).
- [5] C. E. Kim, D.-H. Lim, J. H. Jang, H. J. Kim, S. P. Yoon, J. Han, S. W. Nam, S.-A. Hong, A. Soon, and H. C. Ham, Effect of gold subsurface layer on the surface activity and segregation in Pt/Au/Pt₃M (where $M = 3d$ transition metals) alloy catalyst from first-principles, *J. Chem. Phys.* **142**, 034707 (2015).
- [6] Z. Wang and P. Hu, Formulating the bonding contribution equation in heterogeneous catalysis: A quantitative description between the surface structure and adsorption energy, *Phys. Chem. Chem. Phys.* **19**, 5063 (2017).
- [7] C. M. Kruppe, J. D. Krooswyk, and M. Trenary, Polarization-dependent infrared spectroscopy of adsorbed carbon monoxide to probe the surface of a Pd/Cu(111) single-atom alloy, *J. Phys. Chem. C* **121**, 9361 (2017).
- [8] T. Lee, Y. Lee, S. Piccinin, and A. Soon, *Ab initio* thermodynamics of surface oxide structures under controlled growth conditions, *J. Phys. Chem. C* **121**, 2228 (2017).
- [9] J. A. Rodriguez, Physical and chemical properties of bimetallic surfaces, *Surf. Sci. Rep.* **24**, 223 (1996).
- [10] M. Escudero-Escribano, P. Malacrida, M. H. Hansen, U. G. Vej-Hansen, A. Velázquez-Palenzuela, V. Tripkovic, J. Schiøtz, J. Rossmeisl, I. E. L. Stephens, and I. Chorkendorff, Tuning the activity of Pt alloy electrocatalysts by means of the lanthanide contraction, *Science* **352**, 73 (2016).
- [11] Yong Zhao, Caiyun Wang, and Gordon G. Wallace, Tin nanoparticles decorated copper oxide nanowires for selective electrochemical reduction of aqueous CO₂ to CO, *J. Mater. Chem. A* **4**, 10710 (2016).
- [12] Saad Sarfraz, Angel T. Garcia-Esparza, Abdesslem Jedidi, Luigi Cavallo, and Kazuhiro Takanabe, Cu-Sn bimetallic catalyst for selective aqueous electroreduction of CO₂ to CO, *ACS Catal.* **6**, 2842 (2016).
- [13] E. McLoughlin, A. A. Cafolla, E. AlShamaileh, and C. J. Barnes, A re-interpretation of the Cu/Sn surface phase diagram, *Surf. Sci.* **482**, 1431 (2001).
- [14] A. A. Cafolla, E. McLoughlin, E. AlShamaileh, P. Guaino, G. Sheerin, D. Carty, T. McEvoy, C. Barnes, V. Dhanak, and A. Santoni, Observation of an anti-phase domain structure in the Cu₁₀₀/Sn surface alloy system, *Surf. Sci.* **544**, 121 (2003).
- [15] Y. Nara, K. Yaji, T. Iimori, K. Nakatsuji, and F. Komori, STM observation of surface phases of Sn/Cu(001), *Surf. Sci.* **601**, 5170 (2007).
- [16] K. Yaji, R. Nakayama, K. Nakatsuji, T. Iimori, and F. Komori, Ordered structures of tin-adsorbed Cu(001) surfaces with over monolayer coverage, *Surf. Sci.* **603**, 341 (2009).
- [17] J. Lallo, L. V. Goncharova, B. J. Hinch, S. Rangan, R. A. Bartynski, and D. R. Strongin, Structural studies of sub monolayer Sn/Cu(001) structures, *Surf. Sci.* **602**, 2348 (2008).
- [18] Tetsuya Aruga, Surface Peierls transition on Cu(001) covered with heavier p -block metals, *Surf. Sci. Rep.* **61**, 283 (2006).
- [19] J. D. Fuhr, J. E. Gayone, J. Martínez-Blanco, E. G. Michel, and H. Ascolani, Structural and electronic properties of $(3\sqrt{2} \times \sqrt{2})R45^\circ$ -Sn/Cu(100): Density functional theory and scanning tunneling microscopy, *Phys. Rev. B* **80**, 115410 (2009).
- [20] J. Martínez-Blanco, V. Joco, C. Quiros, P. Segovia, and E. G. Michel, Surface x-ray diffraction analysis using a genetic algorithm: The case of Sn/Cu(100)- $(3\sqrt{2} \times \sqrt{2})R45^\circ$, *J. Phys. Condens. Matter* **21**, 134011 (2009).
- [21] H. Yoshida and H. Tochiwara, Determination of a $p(3\sqrt{2} \times \sqrt{2})R45^\circ$ structure formed by Sn adsorption on Cu(001): A tensor low-energy electron diffraction analysis, *J. Novel Carbon Resour. Sci.* **1**, 29 (2010).
- [22] H. Yoshida, A. Okamoto, S. Mizuno, and H. Tochiwara, Structure determination of the Cu(001)-C(4 × 4)-Sn surface by low-energy electron diffraction, *Surf. Sci.* **604**, 535 (2010).
- [23] M. Walker, M. G. Brown, M. Draxler, M. G. Dowsett, C. F. McConville, T. C. Q. Noakes, and P. Bailey, Structural analysis of the Cu(100)- $p(2 \times 2)$ -Sn surface using low and

- medium energy ion scattering spectroscopies, *Phys. Rev. B* **83**, 085424 (2011).
- [24] M. Lahti, K. Pussi, E. McLoughlin, and A. A. Cafolla, The structure of Cu(100)- $p(2 \times 6)$ -2mg-Sn studied by DFT and LEED, *Surf. Sci.* **605**, 1000 (2011).
- [25] J. Martínez-Blanco, V. Joco, H. Ascolani, A. Tejada, C. Quirós, G. Panaccione, T. Balasubramanian, P. Segovia, and E. G. Michel, Fermi surface gapping and nesting in the surface phase transition of Sn/Cu(100), *Phys. Rev. B* **72**, 041401(R) (2005).
- [26] J. Martínez-Blanco, V. Joco, P. Segovia, T. Balasubramanian, and E. G. Michel, Surface phase diagram and temperature induced phase transitions of Sn/Cu(100), *Appl. Surf. Sci.* **252**, 5331 (2006).
- [27] K. Yaji, R. Nakayama, K. Nakatsuji, T. Iimori, and F. Komori, Phase transition for a 3/8-monolayer Sn-adsorbed Cu(001) bimetallic surface alloy, *Phys. Rev. B* **79**, 115449 (2009).
- [28] K. Pussi, E. Alshamaileh, A. A. Cafolla, and M. Lindroos, Determination of the structure of Cu(100) $p(3\sqrt{2} \times \sqrt{2})R45^\circ$ -Sn by dynamical LEED, *Surf. Sci.* **549**, 24 (2004).
- [29] G. Kresse and J. Furthmüller, Efficiency of *ab initio* total energy calculations for metals and semiconductors using a plane-wave basis set, *Comput. Mater. Sci.* **6**, 15 (1996).
- [30] G. Kresse and J. Furthmüller, Efficient iterative schemes for *ab initio* total-energy calculations using a plane-wave basis set, *Phys. Rev. B* **54**, 11169 (1996).
- [31] P. E. Blöchl, Projector augmented-wave method, *Phys. Rev. B* **50**, 17953 (1994).
- [32] G. Kresse and D. Joubert, From ultrasoft pseudopotentials to the projector augmented-wave method, *Phys. Rev. B* **59**, 1758 (1999).
- [33] J. P. Perdew, K. Burke, and M. Ernzerhof, Generalized Gradient Approximation Made Simple, *Phys. Rev. Lett.* **77**, 3865 (1996).
- [34] H. J. Monkhorst and J. D. Pack, Special points for Brillouin-zone integrations, *Phys. Rev. B* **13**, 5188 (1976).
- [35] See Supplemental Material at <http://link.aps.org/supplemental/10.1103/PhysRevApplied.8.034010> for additional computational details on the change in the Helmholtz free energy of Sn/Cu alloys, energy-volume relations for various Sn allotropes, a comparison of DFT-derived STM images to the corresponding experimentally determined STM measurements, and projected density of states for the Sn/Cu(001) surface structures. Tabulated values for the adsorption energetics, surface work functions, and surface dipole moments for all considered Sn/Cu(001) surface structures in this work are also included in tables.
- [36] A. Soon, M. Todorova, B. Delley, and C. Stampfl, Oxygen adsorption and stability of surface oxides on Cu(111): A first-principles investigation, *Phys. Rev. B* **73**, 165424 (2006).
- [37] X. Duan, O. Warschkow, A. Soon, B. Delley, and C. Stampfl, A density-functional study of oxygen on Cu(100) and Cu(110) surfaces, *Phys. Rev. B* **81**, 075430 (2010).
- [38] A. Soon, L. Wong, M. Lee, M. Todorova, B. Delley, and C. Stampfl, Nitrogen adsorption and thin surface nitrides on Cu(111) from first-principles, *Surf. Sci.* **601**, 4775 (2007).
- [39] J. Tersoff and D. R. Hamann, Theory of the scanning tunneling microscope, *Phys. Rev. B* **31**, 805 (1985).
- [40] D. E. P. Vanpoucke and G. Brocks, Formation of Pt-induced Ge atomic nanowires on Pt/Ge(001): A density functional theory study, *Phys. Rev. B* **77**, 241308(R) (2008).
- [41] C. Kittel, *Introduction to Solid State Physics* (Wiley, New York, 1996).
- [42] J.-H. Lee, J.-H. Park, and A. Soon, Assessing the influence of van der Waals corrected exchange-correlation functionals on the anisotropic mechanical properties of coinage metals, *Phys. Rev. B* **94**, 024108 (2016).
- [43] S.-H. Yoo, J.-H. Lee, Y.-K. Jung, and A. Soon, Exploring stereographic surface energy maps of cubic metals via an effective pair-potential approach, *Phys. Rev. B* **93**, 035434 (2016).
- [44] J. Thewlis and A. R. Davey, Thermal expansion of grey tin, *Nature (London)* **174**, 1011 (1954).
- [45] J. A. Lee and G. V. Raynor, The lattice spacings of binary tin-rich alloys, *Proc. Phys. Soc. London* **67**, 737 (1954).
- [46] N. G. Hörmann, A. Groß, and P. Kaghazchi, Semiconductor-metal transition induced by nanoscale stabilization, *Phys. Chem. Chem. Phys.* **17**, 5569 (2015).
- [47] B. H. Cheong and K. J. Chang, First-principles study of the structural properties of Sn under pressure, *Phys. Rev. B* **44**, 4103 (1991).
- [48] S. N. Vaboya and G. C. Kennedy, Compressibility of 18 metals to 45 kbar, *J. Phys. Chem. Solids* **31**, 2329 (1970).
- [49] J. D. Barnett and V. E. Bean, X-ray diffraction studies on tin to 100 kilobars, *J. Appl. Phys.* **37**, 875 (1966).
- [50] S. Desgreniers, Y. K. Vohra, and A. L. Ruoff, Tin at high pressure: An energy-dispersive x-ray-diffraction study to 120 GPa, *Phys. Rev. B* **39**, 10359 (1989).
- [51] M. Liu and L.-G. Liu, Compressions and phase transitions of tin to half a megabar, *High Temp. High Press.* **18**, 79 (1986).
- [52] C. J. Buchenauer, M. Cardona, and F. H. Pollak, Raman scattering in gray tin, *Phys. Rev. B* **3**, 1243 (1971).
- [53] R. Pentcheva and M. Scheffler, Initial adsorption of Co on Cu(001): A first-principles investigation, *Phys. Rev. B* **65**, 155418 (2002).
- [54] H. Y. Xiao, X. T. Zu, X. He, and F. Gao, Sb adsorption on Cu(110), (100), and (111) surfaces, *Chem. Phys.* **325**, 519 (2006).
- [55] D. F. Li, H. Y. Xiao, X. T. Zu, and H. N. Dong, First-principles study of Sn adsorption on Ni(100), (110) and (111) surfaces, *Mater. Sci. Eng. A* **39**, 50 (2007).
- [56] L. A. Meier and N. J. Castellani, Theoretical study of Sn adsorbed on the Au(111) surface, *Comput. Mater. Sci.* **127**, 48 (2017).
- [57] A. Soon, L. Wong, B. Delley, and C. Stampfl, Morphology of copper particles in a nitrogen atmosphere: A first-principles investigation, *Phys. Rev. B* **77**, 125423 (2008).
- [58] A. Schmalz, S. Aminpirooz, L. Becker, J. Haase, J. Neugebauer, M. Scheffler, D. R. Batchelor, D. L. Adams, and E. Bøgh, Unusual Chemisorption Geometry of Na on Al(111), *Phys. Rev. Lett.* **67**, 2163 (1991).
- [59] C. Stampfl and M. Scheffler, Theory of alkali metal adsorption on close-packed metal surfaces, *Surf. Rev. Lett.* **02**, 317 (1995).
- [60] D. Wortmann, S. Heinze, G. Bihlmayer, and S. Blugel, Interpreting STM images of the MnCu/Cu(100) surface alloy, *Phys. Rev. B* **62**, 2862 (2000).

- [61] M. J. Harrison, D. P. Woodruff, and J. Robinson, Monolayer bimetallic surfaces: Experimental and theoretical studies of trends in electronic and chemical properties, *Phys. Rev. B* **72**, 113408 (2005).
- [62] A. Soon, M. Todorova, B. Delley, and C. Stampfl, Thermodynamic stability and structure of copper oxide surfaces: A first-principles investigation, *Phys. Rev. B* **75**, 125420 (2007).
- [63] J. R. Kitchin, K. Reuter, and M. Scheffler, Alloy surface segregation in reactive environments: First-principles atomistic thermodynamics study of $\text{Ag}_3\text{Pd}(111)$ in oxygen atmospheres, *Phys. Rev. B* **77**, 075437 (2008).
- [64] N. A. Richter, C.-E. Kim, Catherine Stampfl, and A. Soon, Re-visiting the O/Cu(111) system—When metastable surface oxides could become an issue!, *Phys. Chem. Chem. Phys.* **16**, 26735 (2014).
- [65] M. Scheffler and C. Stampfl, in *Handbook of Surface Science: Electronic Structure*, Vol. 2, edited by K. Horn and M. Scheffler (Elsevier, Amsterdam, 2000), Chap. 5, pp. 285–356.

Supplemental Material:

Ab initio surface phase diagram of Sn/Cu(001):

Reconciling experiments with theory

Ji-Hwan Lee,* Jongmin Yun,* Taehun Lee, and Aloysius Soon†

Department of Materials Science and Engineering,

Yonsei University, Seoul 120-749, Korea

(Dated: August 11, 2017)

S1. THERMODYNAMICS OF BULK Sn/Cu ALLOYS

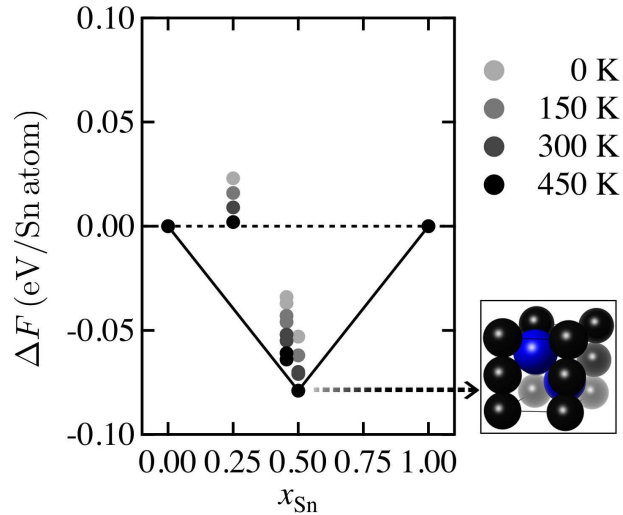


Figure S1. Change in the Helmholtz free energy as function of the mole fraction of Sn (x_{Sn}). The light grey to black markers represent the influence of configuration entropy at various temperatures of 0 K, 150 K, 300 K and 450 K, respectively. For $x_{\text{Sn}} = 1$, the most stable hexagonal SnCu (h -SnCu) bulk alloy is depicted. Here, the black and blue spheres represent Cu and Sn, respectively.

For the mixing enthalpy of bulk alloy systems, we refer to the Helmholtz free energy of mixing (ΔF) according to the following equation,

$$\Delta F = \Delta U - T\Delta S \quad . \quad (1)$$

* These authors contributed equally to this work.

† Corresponding author. E-mail: aloysius.soon@yonsei.ac.kr

The total internal energy (ΔU) is calculated (and approximated) by DFT total energy calculations.

$$\Delta U = E_{\text{Cu}_x\text{Sn}_y} - xE_{\text{Cu}}^{\text{bulk}} - yE_{\text{Sn}}^{\text{bulk}} \quad , \quad (2)$$

where the total energies of bulk *fcc* Cu and *alpha*-Sn are considered.

For the configurational entropy of mixing (ΔS), it is calculated using the Stirling's approximation, where

$$\Delta S = -k_{\text{B}} \left[\frac{x}{x+y} \ln \left(\frac{x}{x+y} \right) - \frac{y}{x+y} \ln \left(\frac{y}{x+y} \right) \right] \quad . \quad (3)$$

Here, k_{B} is the Boltzmann constant.

S2. ALLOTROPES OF BULK Sn

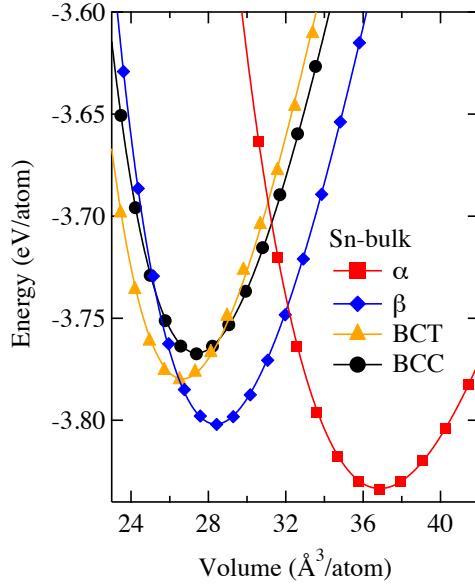


Figure S2. Total energies as a function of atomic volumes are depicted for the four allotropes of Sn. The red square, blue diamond, orange triangle, and black circle markers represent the α , β , body-centered tetragonal (BCT), and body-centered cubic (BCC) phases, respectively. These values are generated via DFT calculations and the solid lines are fitted using the third-order Birch-Murnaghan equation-of-state.

Phase	a_0 (Å)			c_0 (Å)			B_0 (GPa)		
	GGA ^a	LDA ^b	Expt.	GGA ^a	LDA ^b	Expt.	GGA ^a	LDA ^b	Expt.
α	6.65	6.40	6.49 ^c	—	—	—	48.7	51.2	53.0 ^g
β	6.00	5.70	5.83 ^d	3.16	3.11	3.18 ^d	48.3	60.5	57.9 ^h
BCT	3.77	4.79	3.51 ^e	3.74	4.31	3.27 ^e	52.5	57.8	—
BCC	3.80	4.62	3.29 ^f	—	—	—	48.7	57.5	76.4 ⁱ

Table S1. Calculated equilibrium lattice constants (a_0 and c_0) and bulk modulus (B_0) of various Sn allotropes. Here, the GGA-PBE xc -functional is used.

^a Present work.

^b Reference 1.

^c Reference 2.

^g Reference 3.

^d Reference 4.

^h Reference 5.

^e Reference 6.

^f Reference 7.

ⁱ Reference 8.

S3. SURFACE DIPOLE MOMENT (IN DEBYE)

The surface dipole moment can be considered using the concept of a parallel-plate capacitor. The Helmholtz equation, $\mu^{\text{SD}} \propto \Delta\Phi/\Theta$, is used to calculate the surface dipole moment [9, 10], connecting between the surface work function change and the surface dipole moment:

$$\frac{\Delta\Phi(\Theta)}{e} = \frac{\sigma(\Theta)\mu}{\varepsilon_0} \quad , \quad (4)$$

where $\Delta\Phi$ is work-function change with respect to bare surface, σ is a surface density of atom (Θ/A where A is unit surface area), and ε_0 is the vacuum permittivity. Here,

$$\mu = \frac{\varepsilon_0}{\sigma(\Theta)} \cdot \frac{\Delta\Phi(\Theta)}{e} = \frac{\varepsilon_0 A}{\Theta} \cdot \frac{\Delta\Phi(\Theta)}{e} = \frac{A\Delta\Phi(\Theta)}{\mu_0 c_0^2 e \Theta} \quad . \quad (5)$$

Since the vacuum permittivity, ε_0 is equal to the $(\mu_0 c_0^2)^{-1}$ when μ_0 is the vacuum permeability ($4\pi \times 10^{-7}$ H/m) and c_0 is the speed of light in vacuum. Here, for the right-hand side of the equation, considering the unit conversion to Debye,

$$\mu = \frac{A(\text{\AA}^2)}{4\pi \times 10^{-7} \text{ (H/m)}} \cdot \frac{\Delta\Phi(\Theta) \text{ (eV)}}{c_0^2} \cdot \frac{1}{1.602 \times 10^{-19} \text{ (C)}\Theta} \quad , \quad (6)$$

$$\mu = \frac{A\Delta\Phi(\Theta)}{4\pi\Theta} \cdot \frac{1(\text{\AA}^2)}{10^{-7} \text{ (H/m)}} \cdot \frac{1 \text{ (eV)}}{c_0^2} \cdot \frac{1}{1.602 \times 10^{-19} \text{ (C)}} \cdot \frac{10^{20} \text{ (Debye)}}{3.333 \text{ (C} \cdot \text{\AA)}} \quad , \quad (7)$$

where e is 1.602×10^{-19} C and 1 Debye is approximately 3.333×10^{-20} C·Å. In addition, $1 \text{ eV}/c_0^2$ is taken as a mass-value of around 1.783×10^{-36} kg while 1 H (where H is known as the unit ‘Henry’ – the SI for electrical inductance) is taken as $1 \text{ kg} \cdot \text{m}^2/\text{C}^2$ (or $10^{-20} \text{ kg} \cdot \text{\AA}^2/\text{C}^2$).

Therefore, the equation can be rearranged to:

$$\mu = \frac{A\Delta\Phi(\Theta)}{4\pi\Theta} \cdot \frac{1(\text{\AA}^2)}{10^{-7} \text{ (kg} \cdot \text{m}^2/\text{C}^2/\text{m)}} \cdot \frac{1.783 \times 10^{-36} \text{ (kg)}}{1.602 \times 10^{-19} \text{ (C)}} \cdot \frac{10^{20} \text{ (Debye)}}{3.333 \text{ (C} \cdot \text{\AA)}} \quad (8)$$

$$\mu = \frac{A\Delta\Phi(\Theta)}{4\pi\Theta} \cdot \frac{1(\text{\AA})}{10^{-7} \text{ (m)}} \cdot \frac{1.783 \times 10^{-36}}{1.602 \times 10^{-19}} \cdot \frac{10^{20}}{3.333} \text{ (Debye)} \quad (9)$$

$$\mu = \frac{A\Delta\Phi(\Theta)}{4\pi\Theta} \cdot \frac{1.783}{5.339} \text{ (Debye)} \quad (\because 1 \text{ m} = 10^{10} \text{ \AA}), \quad (10)$$

$$\therefore \mu \simeq \frac{A\Delta\Phi(\Theta)}{12\pi\Theta} \text{ (Debye)} \quad . \quad (11)$$

We note that the units of A and $\Delta\Phi$ are taken as \AA^2 and eV, respectively.

S4. CALCULATED PROPERTIES

Label	Θ_{Sn} (ML)	$E_{\text{ad}}^{\text{Sn}}$ (eV/Sn atom)	Φ (eV)	μ^{SD} (Debye)
B	0.063	0.213	4.39	-0.25
B	0.110	0.099	4.29	-0.29
B	0.250	0.059	4.20	-0.20
B	0.500	-0.300	4.37	-0.04
B	0.750	-0.211	4.15	-0.08
B	1.000	0.895	3.72	-0.13
H	0.063	-0.259	4.46	-0.05
H	0.110	-0.369	4.43	-0.08
H	0.250	-0.341	4.30	-0.12
H	0.500	-0.556	4.47	0.00
H	0.750	-0.349	3.98	-0.12
H	1.000	0.844	3.70	-0.14

Table S2. List of the averaged adsorption energy of Sn, $E_{\text{ad}}^{\text{Sn}}$, work function, Φ , and surface dipole moment, μ^{SD} for models with adsorption at two binding sites (B: bridge and H: hollow) Sn/Cu(001) surface structures at the corresponding Sn surface coverage, Θ_{Sn} . The work function of pristine Cu(001) is calculated to be 4.48 eV.

	Surface structure	Θ_{Sn} (ML)	$E_{\text{ad}}^{\text{Sn}}$ (eV/Sn atom)	Φ (eV)	μ^{SD} (Debye)
Figure 2(a)	$c(4 \times 4)$	0.125	-0.925	4.49	0.02
Figure 2(b)	$\begin{pmatrix} 10 & 1 \\ 1 & 10 \end{pmatrix}$	0.162	-0.833	4.48	0.00
Figure 2(c)	$\begin{pmatrix} 2 & 1 \\ 1 & 2 \end{pmatrix}$	0.200	-0.901	4.46	-0.01
Figure 2(d)	$p(2 \times 2)$	0.250	-0.887	4.42	-0.04
Figure 2(e)	$p(6 \times 2)$	0.333	-0.778	4.34	-0.07
Figure 2(f)	$p(6 \times 2)$	0.333	-0.793	4.32	-0.08
Figure 2(g)	$\begin{pmatrix} -2 & 2 \\ 0 & 4 \end{pmatrix}$	0.375	-0.712	4.39	-0.04
Figure 2(h)	$\begin{pmatrix} 2 & 1 \\ 1 & 2 \end{pmatrix}$	0.400	-0.607	4.28	-0.08
Figure 2(i)	$p(6 \times 2)$	0.416	-0.687	4.25	-0.10
Figure 2(j)	$p(3\sqrt{2} \times \sqrt{2})R45^\circ$	0.500	-0.764	4.26	-0.07
Figure 2(k)	$p(\sqrt{2} \times \sqrt{2})R45^\circ$	0.500	-0.621	4.13	-0.12
Figure 2(l)	$p(2 \times 2)$	0.500	-0.625	4.21	-0.09
Figure 2(m)	$\begin{pmatrix} 2 & 1 \\ 1 & 2 \end{pmatrix}$	0.600	-0.351	4.04	-0.13

Table S3. List of the averaged adsorption energy of Sn, $E_{\text{ad}}^{\text{Sn}}$, work function, Φ , and surface dipole moment, μ^{SD} for the Sn/Cu(001) surface models at the corresponding Sn surface coverage, Θ_{Sn} . The work function of pristine Cu(001) is calculated to be 4.48 eV.

	Surface structure	Θ_{Sn} (ML)	$E_{\text{ad}}^{\text{Sn}}$ (eV/Sn atom)	Φ (eV)	μ^{SD} (Debye)
Figure 3(a)	$p(6 \times 2)$	0.333	-0.562	4.26	-0.11
Figure 3(b)	$c(4 \times 4)$	0.500	-0.662	4.32	-0.06
Figure 3(c)	$c(4 \times 4)$	0.625	-0.636	4.09	-0.11
Figure 3(d)	$c(4 \times 4)$	0.625	-0.291	3.88	-0.17
Figure 3(e)	$c(4 \times 4)$	0.625	-0.397	3.86	-0.17
Figure 3(f)	$c(4 \times 4)$	0.750	-0.182	3.94	-0.12
Figure 3(g)	$c(4 \times 4)$	0.750	-0.412	3.84	-0.15
Figure 3(h)	$p(4 \times 4)$	0.750	-0.353	4.10	-0.09
Figure 3(i)	$\begin{pmatrix} 2 & 1 \\ 1 & 2 \end{pmatrix}$	0.800	-0.285	4.11	-0.08
Figure 3(j)	$c(4 \times 4)$	0.875	-0.189	3.79	-0.14
Figure 3(k)	$c(4 \times 4)$	0.875	-0.207	3.79	-0.14
Figure 3(l)	$c(4 \times 4)$	0.875	-0.269	3.90	-0.12
Figure 3(m)	$c(4 \times 4)$	0.938	-0.273	4.07	-0.08
Figure 3(n)	$c(4 \times 4)$	1.000	-0.214	3.73	-0.13

Table S4. List of the averaged adsorption energy of Sn, $E_{\text{ad}}^{\text{Sn}}$, work function, Φ , and surface dipole moment, μ^{SD} for the Sn/Cu(001) surface models at the corresponding Sn surface coverage, Θ_{Sn} . The work function of pristine Cu(001) is calculated to be 4.48 eV.

S5. STM IMAGE

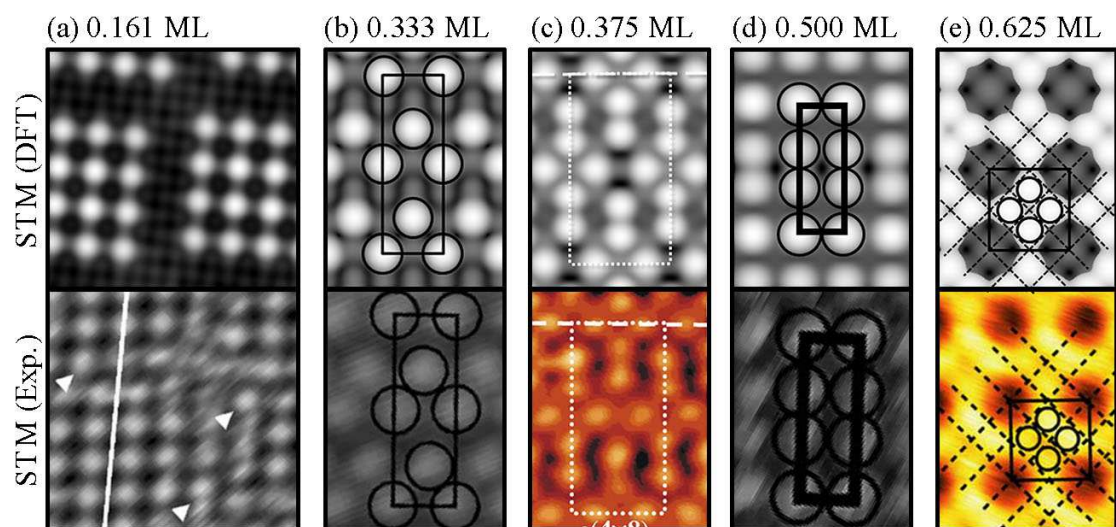


Figure S3. A comparison of the DFT-derived STM images within the Tersoff-Harmann approximation (upper panel) and the corresponding experimentally-determined STM images from References 11–14 (bottom panel).

S6. DENSITY-OF-STATES

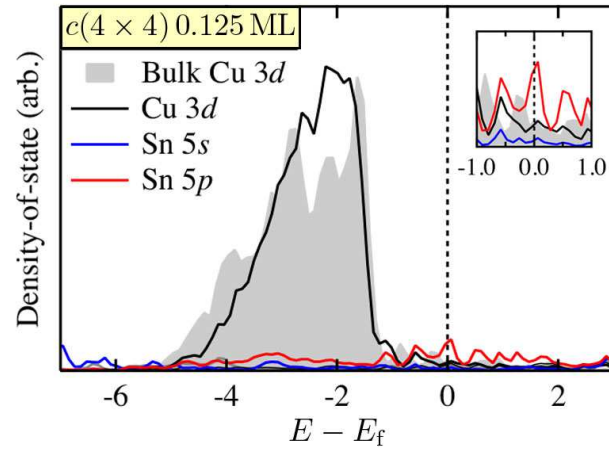


Figure S4. Projected density-of-states for the Sn/Cu(001) $c(4 \times 4)$ -0.125 ML. Here, the Cu atom in the outermost layer and its nearest-neighbor Sn atom is considered.

-
- [1] B. H. Cheong and K. J. Chang, “First-Principles Study of the Structural Properties of Sn under Pressure,” *Phys. Rev. B* **44**, 4103 (1991).
- [2] J. Thewlis and A. R. Davey, “Thermal Expansion of Grey Tin,” *Nature* **174**, 1011 (1954).
- [3] C. J. Buchenauer, M. Cardona, and F. H. Pollak, “Raman Scattering in Gray Tin,” *Phys. Rev. B* **3**, 1243 (1971).
- [4] J. A. Lee and G. V. Raynor, “The Lattice Spacings of Binary Tin-Rich Alloys,” *Proc. Phys. Soc. London* **67**, 737 (1954).
- [5] S. N. Vaidya and G. C. Kennedy, “Compressibility of 18 Metals to 45 Kbar,” *J. Phys. Chem. Solids* **31**, 2329 (1970).
- [6] M. Liu and L.-G. Liu, “Compressions and Phase Transitions of Tin to Half a Megabar,” *High Temp.-High Press.* **18**, 79 (1986).
- [7] J. D. Barnett and V. E. Bean, “X-Ray Diffraction Studies on Tin to 100 Kilobars,” *J. Appl. Phys.* **37**, 875 (1966).
- [8] S. Desgreniers, Y. K. Vohra, and A. L. Ruoff, “Tin at High Pressure: An Energy-Dispersive X-Ray-Diffraction Study to 120 GPa,” *Phys. Rev. B* **39**, 10359 (1989).
- [9] A. Soon, M. Todorova, B. Delley, and C. Stampfl, “Oxygen Adsorption and Stability of Surface Oxides on Cu(111): A First-Principles Investigation,” *Phys. Rev. B* **73**, 165424 (2006).
- [10] X. Duan, O. Warschkow, A. Soon, B. Delley, and C. Stampfl, “A Density-Functional Study of Oxygen on Cu(100) and Cu(110) Surfaces,” *Phys. Rev. B* **81**, 075430 (2010).
- [11] Y. Nara, K. Yaji, T. Iimori, K. Nakatsuji, and F. Komori, “STM Observation of Surface Phases of Sn/Cu(001),” *Surf. Sci.* **601**, 5170 (2007).
- [12] J. Lallo, L. V. Goncharova, B. J. Hinch, S. Rangan, R. A. Bartynski, and D. R. Strongin, “Structural Studies of Sub Monolayer Sn/Cu(001) Structures,” *Surf. Sci.* **602**, 2348 (2008).
- [13] H. Yoshida, A. Okamoto, S. Mizuno, and H. Tochiyama, “Structure Determination of the Cu(001)-c(4×4)-Sn Surface by Low-Energy Electron Diffraction,” *Surf. Sci.* **604**, 535 (2010).
- [14] K. Yaji, R. Nakayama, K. Nakatsuji, T. Iimori, and F. Komori, “Ordered Structures of Tin-Adsorbed Cu(001) Surfaces with Over Monolayer Coverage,” *Surf. Sci.* **603**, 341 (2009).